REPORT DOCUMENTATION PAGE

Public reporting burden for this collection of information is estimated to average 1 hour per response, including the time for reviewing instructions, searching existing data sources, gathering and maintaining the data needed, and completing and reviewing this collection of information. Send comments regarding this burden estimate or any other aspect of this collection of information, including suggestions for reducing this burden to Department of Defense, Washington Headquarters Services, Directorate for Information Operations and Reports (0704-0188) 1215 Jefferson Davis Highway, Suite 1204, Arlington, VA 22202-4302. Respondents should be aware that notwithstanding any other provision of law, no person shall be subject to any penalty for failing to comply with a collection of information if it does not display a currently valid OMB control number. **PLEASE DO NOT RETURN YOUR FORM TO THE ABOVE ADDRESS.**

1. REPORT DATE (DD-MM-YYYY)	2. REPORT TYPE	3. DATES COVERED (From - To)
		1 SEP 02-31 AUG 03

4. TITLE AND SUBTITLE

EXPLOITATION OF OMNIDIRECTIONAL REFLECTIVITY

5a. CONTRACT NUMBER
F49620-02-C-0089

5b. GRANT NUMBER

5c. PROGRAM ELEMENT NUMBER

6. AUTHOR(S)

M. SKOROBOGATHY

5d. PROJECT NUMBER

5e. TASK NUMBER

5f. WORK UNIT NUMBER

7. PERFORMING ORGANIZATION NAME(S) AND ADDRESS(ES)

OMNIGUIDE COMMUNICATIONS INC.
ONE KENDALL SQ. BLDG. 100
CAMBRIDGE, MA 02139

8. PERFORMING ORGANIZATION REPORT

20040105 091

9. SPONSORING / MONITORING AGENCY NAME(S) AND ADDRESS(ES)
AFOSR/NM
4015 Wilson Blvd., Room 713
Arlington, VA 22203-1954

10. SPONSOR/MONITOR'S ACRONYM(S)
F49620-02-C-0089

11. SPONSOR/MONITOR'S REPORT NUMBER(S)

12. DISTRIBUTION / AVAILABILITY STATEMENT

APPROVED FOR PUBLIC RELEASE, DISTRIBUTION UNLIMITED

AFRL-SR-AR-TR-03-
0513

13. SUPPLEMENTARY NOTES

14. ABSTRACT

In Phase I we developed an extensive set of tools to simulate the performance of Omni-Guide fibers; hollow, high POWER transmission fibers employing an omni-directional dielectric minor as the confining mechanism. Separately, we have experimentally confirmed the validity of many of the tools. Our theoretical/numerical analysis of field propagation through Omni Guide fibers addressed several major design aspects (Fig. 1.1.). Objectives for the tools we developed were as follows:

1. Optimal design of Omni Guide fibers, including reduction of absorption and radiation losses.
2. Assessment of coupling efficiency between the high power lasers and the guided modes of an Omni Guide fiber.
3. Determination of beam quality degradation (M2) due to the inter-modal scattering caused by bends and other fiber imperfections, including diameter and ellipticity variations along the fiber.
4. Determination of the thermal stability of the fibers including equilibrium and non-equilibrium temperature distributions across the fiber due to CW and pulsed sources. Study of the effects of bends and other geometrical variations on fiber heating.
5. Analysis of devices based on Omni Guide fibers using the Beam Propagation Method.

15. SUBJECT TERMS

16. SECURITY CLASSIFICATION OF:			17. LIMITATION OF ABSTRACT	18. NUMBER OF PAGES	19a. NAME OF RESPONSIBLE PERSON
a. REPORT	b. ABSTRACT	c. THIS PAGE		38	19b. TELEPHONE NUMBER (include area code)

FINAL REPORT

AFOSR Phase I Contract Number F49620-02-C-0089

DESIGN AND SIMULATION OF TRANSMISSION PROPERTIES OF HOLLOW BRAGG FIBERS FABRICATED FROM OMNIDIRECTIONALLY REFLECTIVE COMPOSITE DIELECTRIC MATERIALS

M. Skorobogatiy, Steven A. Jacobs, Yoel Fink

OmniGuide Communictions Inc., One Kendall Sq., Build. 100

Cambridge, MA 02139

During our phase I effort, we have developed a wide range of tools to simulate the performance of photonic bandgap fibers (PBFs) and related structures. Many of the theoretical results have been verified using experimental data from in-house measurements. This final report summarizes our phase I progress.

3

1 Phase I Technical objectives and accomplishments

In Phase I we developed an extensive set of tools to simulate the performance of OmniGuide fibers: hollow, high power transmission fibers employing an omnidirectional dielectric mirror as the confining mechanism. Separately, we have experimentally confirmed the validity of many of the tools. Our theoretical/numerical analysis of field propagation through OmniGuide fibers addressed several major design aspects (Fig. 1.1). Objectives for the tools we developed were as follows:

1. Optimal design of OmniGuide fibers, including reduction of absorption and radiation losses.

2. Assessment of coupling efficiency between the high power lasers and the guided modes of an OmniGuide fiber.

3. Determination of beam quality degradation (M^2) due to the inter-modal scattering caused by bends and other fiber imperfections, including diameter and ellipticity variations along the fiber.

4. Determination of the thermal stability of the fibers including equilibrium and non-equilibrium temperature distributions across the fiber due to CW and

4

pulsed sources. Study of the effects of bends and other geometrical variations on fiber heating.

5. Analysis of devices based on OmniGuide fibers using the Beam Propagation Method

In other efforts, we have analyzed the conversion efficiency between the fundamental mode of a low power laser and the lowest loss TE_{01} mode of an OmniGuide fiber ($HE_{11} \rightarrow TE_{01}$ modal converters).
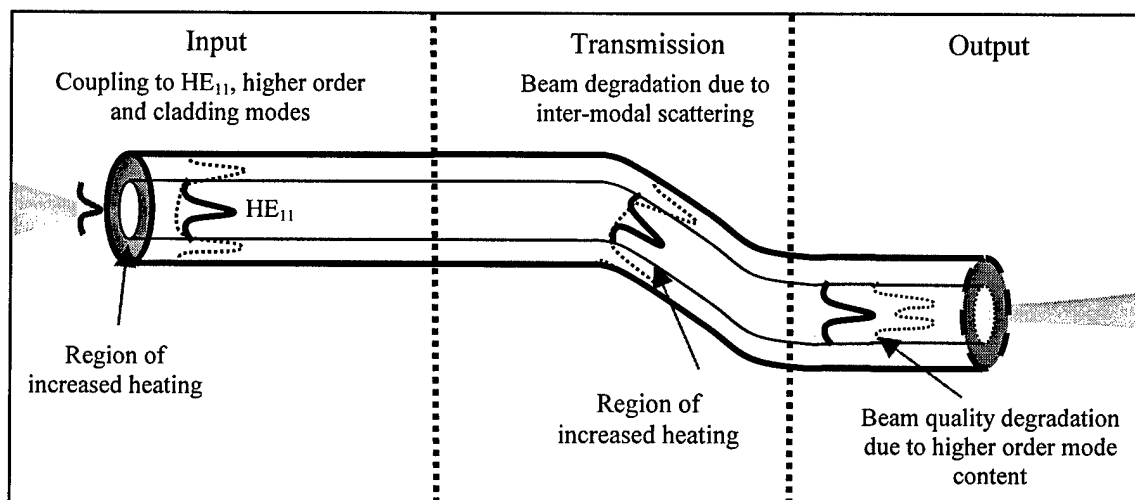
Figure 1.1. Major areas of theoretical analysis in high power fiber design. Input - coupling efficiency, end face heating; Transmission – index profile design and optimization, scattering/radiation due to imperfections/bends, excess heating due to bends; Output -beam quality M^2 estimation.

1.1 Tools developed during Phase I

During phase I, the following tools were developed:

1) For idealized systems we developed:

   a. Software to calculate the band structure of a multilayer planar reflector using the transfer matrix method[1,2,4-7].

   b. Software to calculate the band structure of a cylindrically symmetrical waveguide with a generalized multilayer dielectric structure[3,8-10] using transfer matrix[3] and Galerkin type methods.

2) For high index contrast systems slightly different (or perturbed) from the geometrically ideal systems, we have developed several computationally efficient perturbation theories[11,13,14] to determine :

    a. Radiation absorption by the lossy dielectric media.

    b. Effects of waveguide nonlinearities.

    c. Propagation constants (real parts of the effective indexes) of the modes of a dielectric waveguide due to an arbitrary geometrical perturbation of its structure.

    d. Inter-mode coupling due to an arbitrary geometrical perturbation of a waveguide structure, including polarization mode dispersion (PMD).

    e. Scattering loss in a hollow OmniGuide fiber due to the roughness of the reflector's surface.

    f. Changes in the modal radiation loss due to the perturbations in reflector's geometry.

    g. Scattering losses due to the roughness of the reflector's surface.

    h. Radiation along slightly non-uniform waveguides (propagation-direction dependent perturbation theory).

3) For OmniGuide fibers with lossy dielectrics a numerical tool was created based on the Galerkin method to calculate complex propagation constants. Furthermore, this software was extended to calculate increased modal loss in bent[12] waveguides.

4) A Galerkin-type numerical tool was developed to characterize coupling between the modes of an OmniGuide fiber and a Gaussian laser source.

5) To determine power capacity, heat flow equations were solved with a heat source obtained from absorption of electromagnetic energy during field propagation through a fiber. Temperature rise was computed for CW and pulsed sources, and for straight and bent fibers.

6) For the optimization of omnidirectional reflectors, tools based on nonlinear Newton, conjugate gradient, and non-gradient based numerical optimization

methods were developed for the automated design of planar multi-reflectors and OmniGuide fibers to obtain:

   a. Maximum width omni-directional frequency windows.

   b. Minimized absorption and radiation losses.

   c. Tailored dispersion and reduced PMD.

7) To analyze radiation transmission along a generic imperfect waveguide, software implementing the Beam Propagation Method (BPM) was developed. Stability of the software was demonstrated even for high index contrast waveguides.

1.2 Refining of theoretical tools using in-house *experimental data*

Adjustments and fine tuning of analytical models and numerical software were made throughout the program based on extensive experimental data from our in-house laboratories.

2 Major toolboxes developed during phase I

Numerical tools developed in Phase I allow us to perform comprehensive analyses of all critical aspects of OmniGuide fiber design and optimization.

In the following we describe the major toolboxes, their capabilities, and input and output data streams. We demonstrate their utility by analyzing some typical OmniGuide fiber designs.

Toolboxes developed during phase I	
Toolbox function	Toolbox input/output
Optimal design of OmniGuide fiber. Characterization of modal radiation and absorption losses. Optimal fiber geometry design for high power applications with reduced loss.	Input: material parameters (indexes of refraction and bulk material absorption losses), core radius, number of layers. Output: optimized individual layer thicknesses and corresponding losses.
Laser to fiber coupling efficiency analysis. Characterization of excited fiber modes in a coupler; mediated coupling between high power laser and hollow Bragg fibers.	Input: coupler and waveguide geometries, material parameters, diameter of the incoming Gaussian laser beam. Output: losses in the coupler, modal excitation coefficients.
Analysis of fiber performance degradation due to geometric imperfections. Characterization of increased modal loss	Input: fiber geometry, material parameters. Imperfections parameters – radius of curvature and bend angle (bends),

due to generic planar bends and fiber diameter fluctuations.	amplitude of variations as a function of propagation length (diameter fluctuations). Output: amplitudes of the excited modes after the imperfection region. Loss.
Calculation of outgoing beam quality (M^2) Outgoing beam is propagated from the fiber end facet through free space and compared with Gaussian beam divergence.	Input: fiber geometry, material parameters, amplitudes of excited fiber modes. Output: electromagnetic fields at the specified distance from the output fiber facet and estimates of the M^2 from beam divergence fit.
Temperature distribution in hollow Bragg fibers due to CW and pulsed sources. Calculation of stationary and time dependent temperature rise along the fiber for arbitrary modal excitation pattern.	Input: fiber geometry, material parameters, amplitudes of excited modes along the length of a fiber, CW or pulse parameters of an incoming laser. Output: temperature rise along the fiber at any point inside the fiber.
$HE_{11} \rightarrow TE_{01}$ modal converter design. Calculates efficiency of conversion into the lowest loss TE_{01} mode.	Input: fiber geometry. Parameters of the serpentine mode converter – pitch, amplitude, length of the incoming and outgoing regions. Output: amplitudes of excited modes.
Beam Propagation Method. Modeling of long distance radiation propagation along the waveguide in the presence of slow varying imperfections.	Input: fiber and slow imperfections geometry along the direction of propagation. Incoming profile of the electromagnetic fields. Output: profile of outgoing electromagnetic fields.

2.1 Toolbox: optimal design of OmniGuide fibers

Input: material parameters including indices of refraction, bulk material absorption losses, hollow core radius, number of mirror layers.

Output: optimized individual layer thicknesses and corresponding fiber radiation and absorption losses.

Using in-house transfer matrix software we first design a planar multilayer dielectric omnidirectional reflector and then employ that design to make a cylindrical internal reflecting surface to confine radiation in a fiber core. The simplest planar reflector design employs a constant period where thicknesses of high and low index layers are fixed

across the reflector. Although the most intuitive and well-studied, such reflectors exhibit suboptimal losses at their wavelength of maximum reflection.

We developed a design code that optimizes the thicknesses of each individual reflector layer so that the total reflection off a planar stack is maximized for ½ TM, ½ TE (HE$_{11}$-like) polarization of incoming radiation. After an initial optimization of the planar reflector, we adopt the same layer thicknesses for the dielectric mirror of an OmniGuide fiber. Finally, we run another optimization code that fine-tunes the dielectric layer thicknesses of the reflector in the fiber geometry.

The result of the optimization process is a dramatic reduction in the losses of the OmniGuide fiber, compared to an unoptimized design.

In all the examples below we will use materials[15] currently under investigation at OmniGuide Communications Inc. (OGCI)

2.1.1 Example of toolbox application: optimal design of chalco-polymer mirror, polymer cladding system

In Progress Reports I and II we considered a chalco-polymer-polymer design with the following structural parameters. The core radius R_i is chosen to be 500 μm. The mirror materials are chosen to be a chalcogenide glass (high index) and a polymer (low index) with indices of n$_l$ = 1.5 and n$_h$ = 2.8, with a bi-layer thickness, d=2.82 μm. The corresponding material layer thicknesses are 1.97 μm and 0.84 μm, respectively. The intrinsic bulk absorption loss of the high index material is 10 dB/m, an overestimate for high purity chalcogenide glasses at λ = 10.6 μm. The cladding and low index material are assumed to have absorption loss of 10^{5}dB/m, typical of polymers. We assume a mirror of 35 layers (17.5 bi-layers), thus R_m = 549 μm. At λ=10.6 μm, these structural parameters produce *an unoptimized fiber radiation loss of 8.9 dB/km* (with a radiation loss decreasing by 10X with every 4 bi-layers added), *and an absorption loss of 313.6 dB/km.*

Next, the first five layer thicknesses are optimized to reduce the absorption in the polymer material, and, starting with the chalco layer, they are chosen by the optimization software to be 0.51 μm, 0.97 μm, 1.52 μm, 0.97 μm, and 1.52 μm. At λ=10.6 μm, these optimized structural parameters *produce a fiber radiation loss of 3.4 dB/km* (with a radiation loss decreasing by 10X with every 4 bi-layers added), *and an absorption loss of*

79 dB/km. Thus, optimization reduces the total fiber loss by a factor of 4 as demonstrated in Fig. 2.1.1.

HE$_{11}$ dissipation losses for R$_c$=500μm, N$_l$=35, n$_h$/n$_l$=2.8/1.5, λ$_{op}$=10.6μm
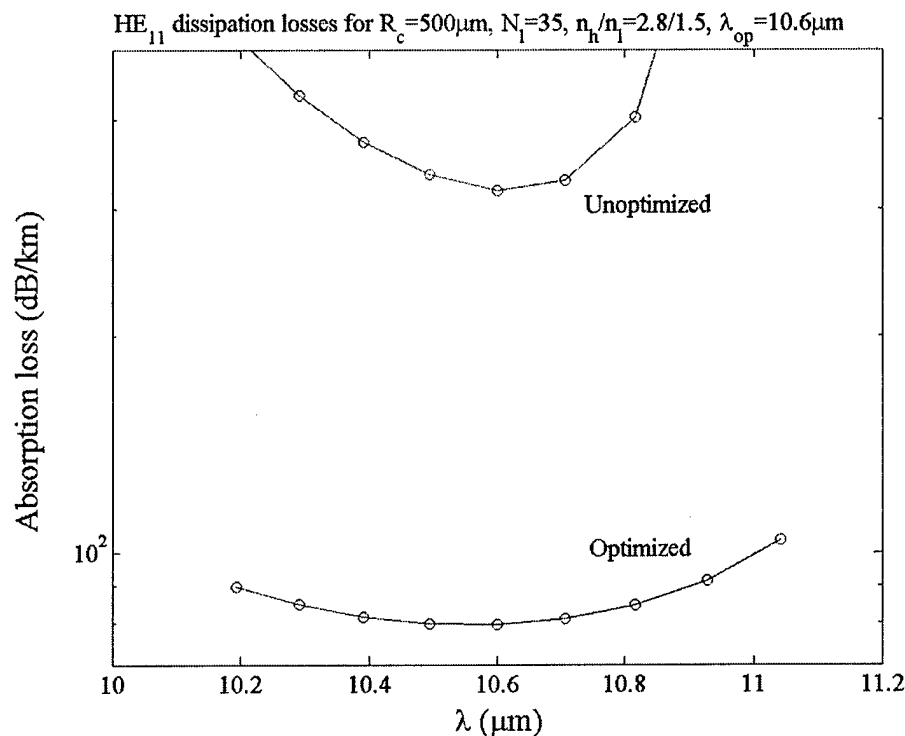
Figure 2.1.1 Absorption loss of the chalco-polymer-polymer fiber as a function of the wavelength. For comparison, losses of the unoptimized and optimized structures are presented.

2.2 Toolbox: coupling between high power laser and OmniGuide fibers

Input: coupler and waveguide geometries, material parameters, diameter of the incoming Gaussian laser beam. Coupler is modeled as a lossy metallic tube butt-coupled to the fiber. Coupler and fiber centers are aligned. Focus of the incoming Gaussian can be located anywhere along the fiber axis.

Output: losses in the coupler, modal excitation coefficients in the fiber.

In this toolbox we analyze coupling from a Gaussian laser beam to an OmniGuide fiber, shown schematically in Fig. 2.2.1. The output from a laser passes through a lens

and is focused to a spot of width w_0, at either the fiber endface or elsewhere along the fiber axis. From this analysis we predict the amplitudes of modes excited in the fiber.

The incident laser beam, assumed to have a Gaussian profile, is decomposed into a sum of forward-propagating modes of a homogeneous waveguide, and the reflected field is expressed as a sum of backward-propagating modes. Similarly, the field in the fiber is expressed as a sum over forward-propagating fiber modes. The amplitudes of these modes are chosen so that the electric and magnetic fields satisfy the proper continuity conditions on the fiber endface. The beam parameters are then varied to optimize the coupling efficiency.
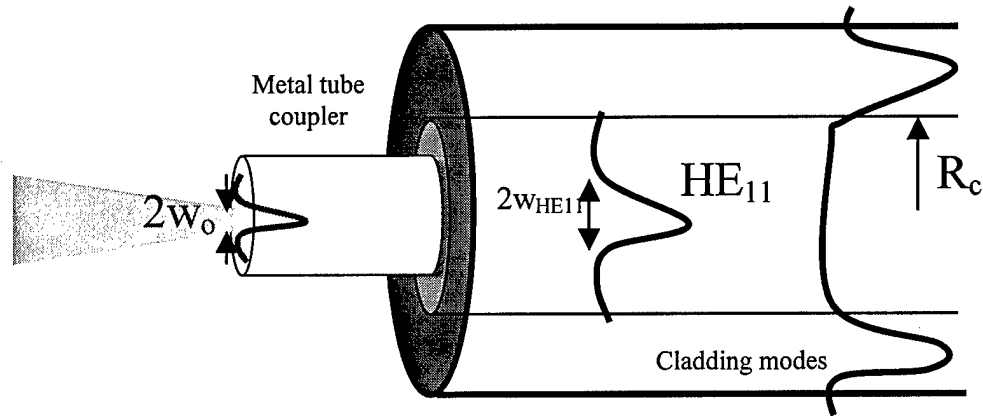

Figure 2.2.1. Geometry of the coupling between laser beam and an OmniGuide fiber. Due to a non- zero overlap between the incoming Gaussian and the mirror, highly dissipative cladding modes could be excited, and an intermediate aperture may be necessary.

2.2.1 Example of toolbox application: optimal coupling to the chalco-polymer mirror, polymer cladding system

At a wavelength of 10.6 microns, we consider coupling to a 35 layer OmniGuide fiber with $n_{hi} = 2.8$, $n_{lo} = 1.6$, a core radius of 500 microns, and a bilayer thickness 2.82 microns. The coupling efficiency from a laser beam to the HE11 core mode of this fiber is shown in Fig. 2.2.2, below, as a function of the beam spotsize w_0. In this example, the beam was focused directly on the fiber endface (i.e., $z_0 = 0$). From the figure, we see that a maximum coupling efficiency of 98.6 % can be obtained from a beam with $w_0 = 235$

µm. With this beam, only 0.05 % of the incident power is reflected; the remainder of the incident beam excites undesired modes of the fiber.
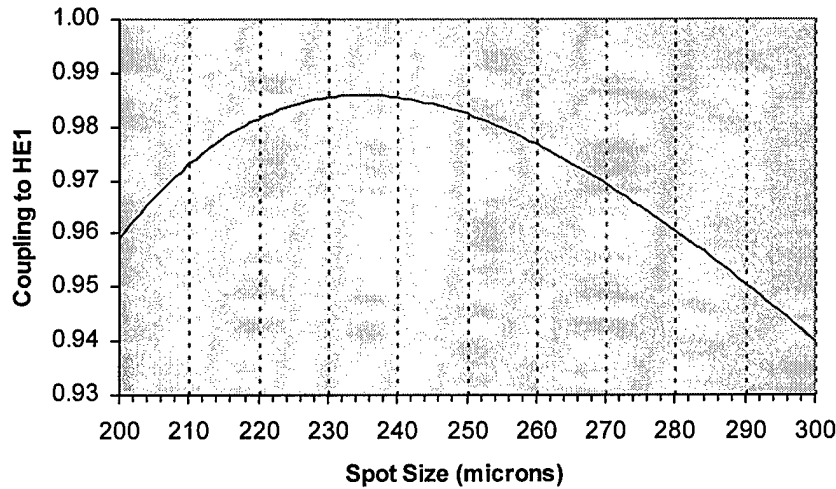

Figure 2.2.2. Coupling efficiency from a laser beam to the HE11 mode of OGCI fiber as a function of the spotsize of the beam.

However, in Progress Report II we established that a more appropriate condition for optimal coupling is a reduction in the excitation of the cladding (polymer) modes (Fig. 2.2.3), to reduce heating in the polymer cladding. This usually leads to a suboptimal coupling to the HE_{11} mode at the point of the lowest fiber end heating. Thus, although an optimal Gaussian spot size is 235µm for the optimal coupling to the HE_{11} mode, coupling to the cladding modes is still very strong (on the order of 10^{-3} of the incident power). In the following analysis, we show that power coupled to the cladding modes should be reduced below 10^{-6} of the incident power to reduce the fiber end heating below acceptable values. For that, the largest spot size we can tolerate without deliberately shielding the fiber end is 140µm, at which point the coupling to the HE_{11} mode is still quite large and equal to 65%. We also established and successfully tested simple scaling laws that approximate the coupling efficiencies to the HE_{11} and cladding modes. These laws are derived assuming a Gaussian HE_{11} field profile of effective width $w_{HE11}=235$µm, and exponential decay of the fields of an incoming Gaussian laser beam in the cladding region of the fiber. With these assumptions, we find that

12

$$P_{HE_{11}} = P_{HE11}^{max} \left(\frac{2 w_{HE11} w_0}{w_{HE11}^2 + w_0^2} \right)^2 \qquad P_{clad} = \exp\left[-\left(R_c / w_0 \right)^2 \right]$$
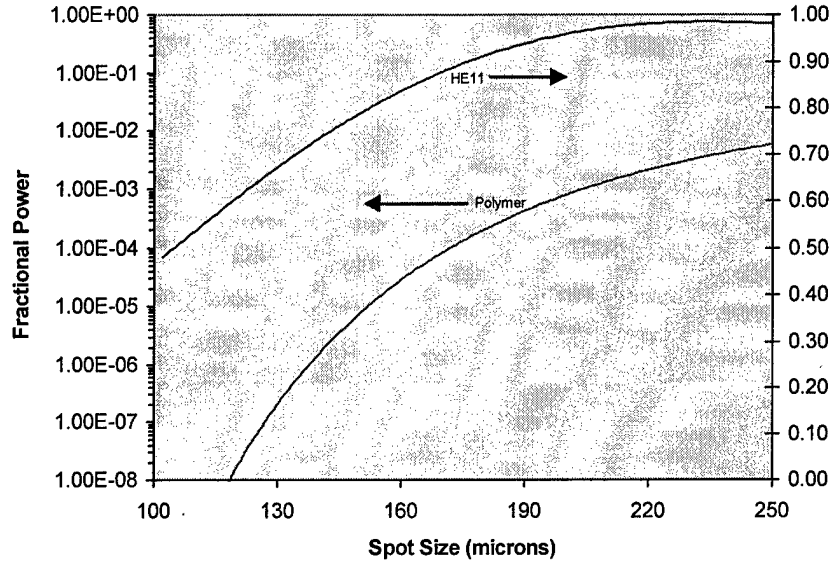

Figure 2.2.3. Coupling to the HE11 and cladding (polymer) modes of the chalco-polymer-polymer design as a function of the incoming Gaussian spot size.

2.3 Toolbox: modeling increased modal loss due to generic planar bends and diameter variations

Input: fiber geometry, material parameters, description of imperfection. The imperfection

parameters for bending loss calculations: radius of curvature and bend angle; for

diameter fluctuations: amplitude of diameter variation along propagation length.

Output: amplitudes of the excited modes inside and after the imperfection region, total

loss due to the imperfections.

This toolbox models the degradation of a field propagating through either a bend or a region with diameter fluctuations. This degradation generally results from scattering from the incident fundamental mode into the higher order guided modes and the radiation continuum. Such scattering leads to an additional loss, as well as an increase in the beam M^2. We developed a software tool based on coupled mode theory with absorbing boundary conditions that calculates fiber losses under such variations, and successfully verified it against experimental data.

13

2.3.1 Example of toolbox application: bend losses in hollow metal fibers (comparison with experiment) and OmniGuide fibers

In Figs. 2.3.1, 2.3.2, and 2.3.3 we present calculations of the straight and bend losses of a hollow metallic (silver) fiber with a single dielectric layer (silver iodide), along with experimental data from Matsuura[16]. In these simulations, the index of refraction of silver is taken to be $13.5 + 75.3i$ (Miyagi and Kawakami) and the index of refraction of the silver iodide layer is 2.1. The silver iodide layer has a thickness of 0.6 μm. We observe excellent agreement between the theoretical predictions and the experimental data.
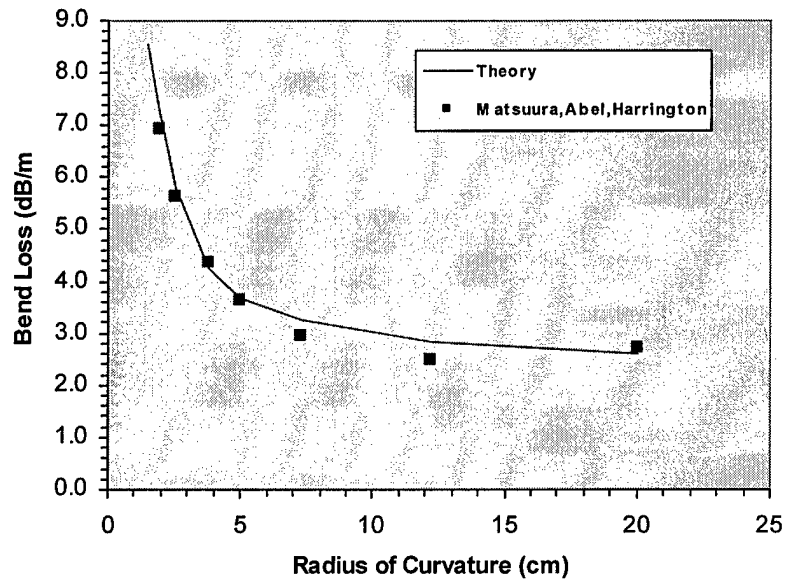

Figure 2.3.1. Predicted and measured HE_{11} mode loss of a straight waveguide as a function of fiber core radius.

Figure 2.3.2. Core radius = 125 μm. Predicted and measured bend loss as a function of the bend curvature. $E \perp$ to plane of the bend. Measured for a 90° bend.
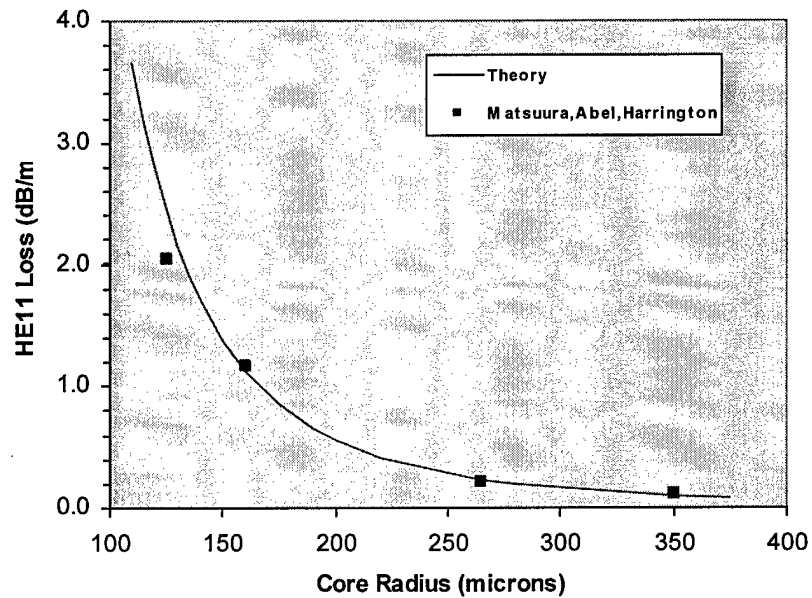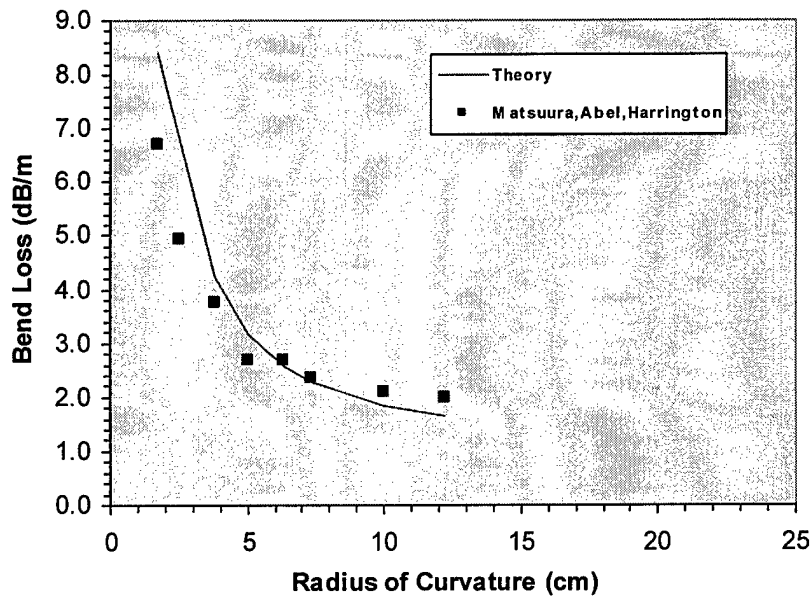

Figure 2.3.3. Core radius = 160 μm. Predicted and measured bend loss as a function of the bend curvature. $E \perp$ to plane of the bend. Measured for a 90° bend.

In Fig. 2.3.4 we present the bending losses after a 90° circular bend in the unoptimized OmniGuide fiber (described above) as a function of its core radius, for three different values of curvature radii. For the optimized design, bending losses improve dramatically. In Fig. 2.3.5 we compare bending losses after a 90° circular bend of radius 20cm between the optimized and unoptimized designs.

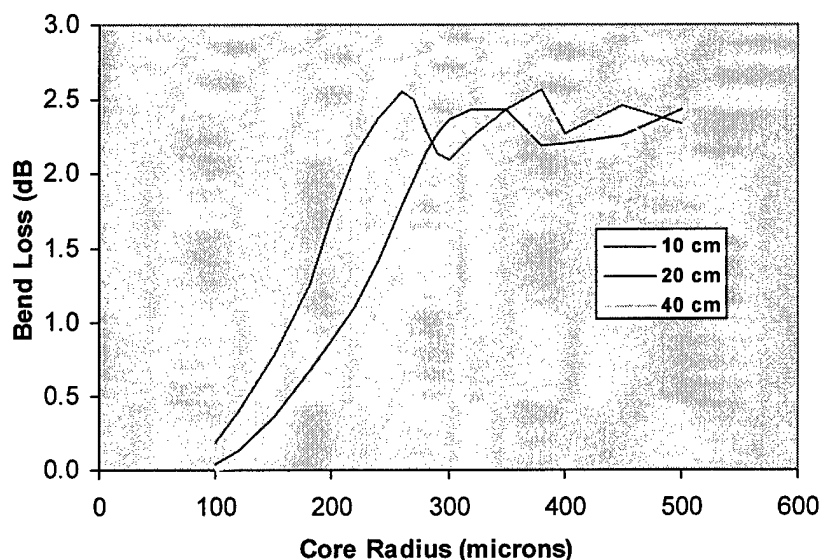Figure 2.3.4. Core radius = 160 µm. Predicted and measured 90^0 bend loss as a function of the core radius. $E \perp$ to plane of the bend.
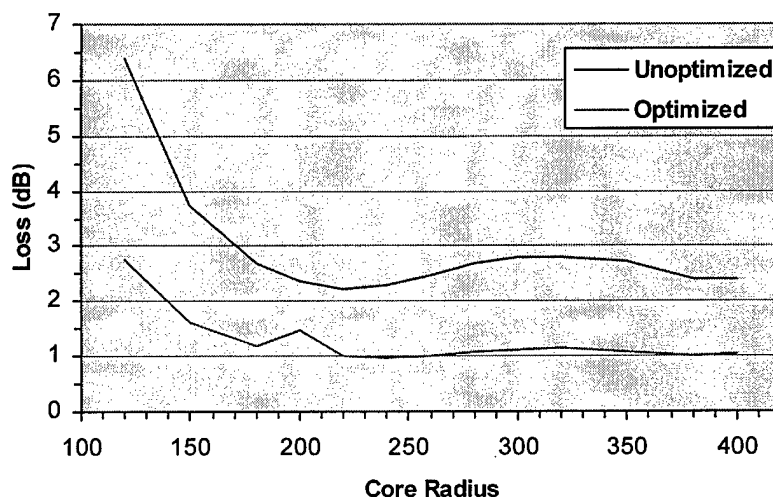

Figure 2.3.5. Predicted total loss (linear plus bending) for chalco-polymer-polymer OGCI fiber as a function of the core radius. $E \perp$ to plane of the bend. Simulation for a 90°

16

bend, and 20cm radius of curvature. The unoptimised design from Report I is compared to an optimized design presented in the current report. Total loss is much smaller for the optimized design, for any value of the core radius.

2.4 Toolbox: calculation of spatial beam quality - M^2

Input: fiber geometry, material parameters, amplitudes of excited fiber modes at the fiber output facet.

Output: electromagnetic fields at a specified distance from the output fiber facet and estimates of the M^2 from the beam divergence.

Degradation of a field propagating through a bent fiber is frequently characterized by the M^2 number. The degradation arises from inter-modal scattering between the initial fundamental mode and the higher order modes. Such scattering leads to an increase in the output beam diameter, an increase in the angle of beam divergence, and "speckling" of the radiation profile.

One standard measure of the beam quality is the M^2 number, which can be defined through the divergence of the beam diameter D(z) once light leaves the fiber. This measure ultimately reflects the smallest spot size that an outgoing beam can be focused to. In the Gaussian beam approximation, the beam diameter is given by

$$D_{M^2}^2(z) = D^2(0)\left[1 + \left(\frac{4M^2\lambda z}{\pi D^2(0)}\right)^2\right]^{\frac{1}{2}}$$

We obtain M^2 by fitting $D_{M^2}(z)$ to the exact divergence D(z).

We evaluate the beam diameter D(z) by numerically propagating the field from the output of a fiber to a distance L (usually several cm) until a reliable determination of M^2 is achieved. Given the field intensity I(r,z), the beam diameter is defined as

$$D(z) = 2\sqrt{2}\left[\frac{\oiint r^2 I(r,z)dA}{\oiint I(r,z)dA}\right]^{\frac{1}{2}},$$

The beam quality parameter M^2 is obtained by minimizing the discrepancy Q between the Gaussian approximation and D(z) along the propagation length L:

$$Q = \int_0^L \left[D^2(0) \left[1 + \left(\frac{4M^2 \lambda z}{\pi D^2(0)} \right)^2 \right]^{\frac{1}{2}} - D(z) \right]^2 dz .$$

2.4.1 Example of toolbox application: M^2 of major propagating modes

In the following, we present results of the evaluation of M^2 for several low-order modes in an OmniGuide fiber of the chalco-polymer-polymer design. The fiber is composed of 20 bilayers, and has a core ID of 660μm, and an OD of 1250μm. In Fig. 2.4.1 we show the calculated divergence of the TE_{01} mode after it exits the fiber.

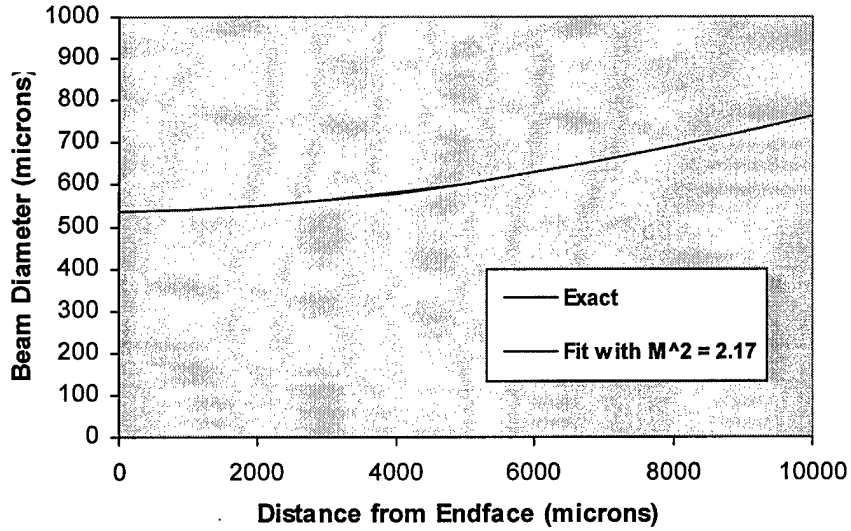Figure 2.4.1. Exact beam diameter D(z) and the beam optics approximation $D_{M^2}(z)$ for the TE_{01} mode of optimized fiber. For this mode, M^2=2.17.

The following table provides the M^2 numbers for some of the main modes of interest of this OmniGuide fiber

HE11	TE01	HE21	HE12	EH11	EH21
1.10	2.17	2.17	3.02	3.22	4.26

2.5 Toolbox: heat dissipation in OmniGuide fibers due to CW and pulsed sources; calculation of the fiber power capacity

Input: fiber geometry, material parameters, amplitudes of excited modes along the length of a fiber, CW or pulsed source parameters of the incoming laser beam.

Output: temperature rise along the fiber at any point inside the fiber. Possible fiber configurations include straight, straight with a coupler, bent.

This toolbox calculates the stationary temperature distribution along the fiber due to a CW source, and the peak temperature distribution along the fiber due to a pulsed laser source. We developed a rigorous solver of the heat-transfer equations with exact heat sources due to absorption of electromagnetic energy in the fiber material. This solver also allows investigation of heating due to imperfect laser-fiber coupling, and fiber bends.

In general, an OmniGuide fiber consists of a hollow core surrounded by alternating layers of materials with high and low indices of refraction. Fig. 2.5.1 (a) illustrates the cross section of the fiber. Light is guided primarily in the hollow core of radius R_i by means of the dielectric mirror having N dielectric bi-layers each of thickness d extending to the radius R_m. Outside of the mirror there is a cladding of radius R_o.

The mirror is designed in such a way that, for a given frequency, the modal fields decay exponentially in the mirror region. Thus, field penetration into the mirror is limited largely to the first few bi-layers. Moreover, as the core area is 100-1000 times larger than the mirror area, power dissipation in the mirror due to the material absorption is greatly suppressed. In the following, we refer to the power dissipated in the first few bi-layers of the mirror due to the finite modal field penetration as H_{abs} (Fig. 2.5.1 b)).

Another source of power dissipation is absorption of the radiation leaking from the finite-sized mirror. This radiation will be mostly converted to heat in the over clad region. The radiated power dissipated in this region is defined as H_{rad}. Fibers can be built that can withstand kilowatts of transmitted power, even without forced cooling, by designing them so that most of the energy propagates in the hollow core, minimal energy propagates in the mirror, and minimal radiation leaks into the over clad.
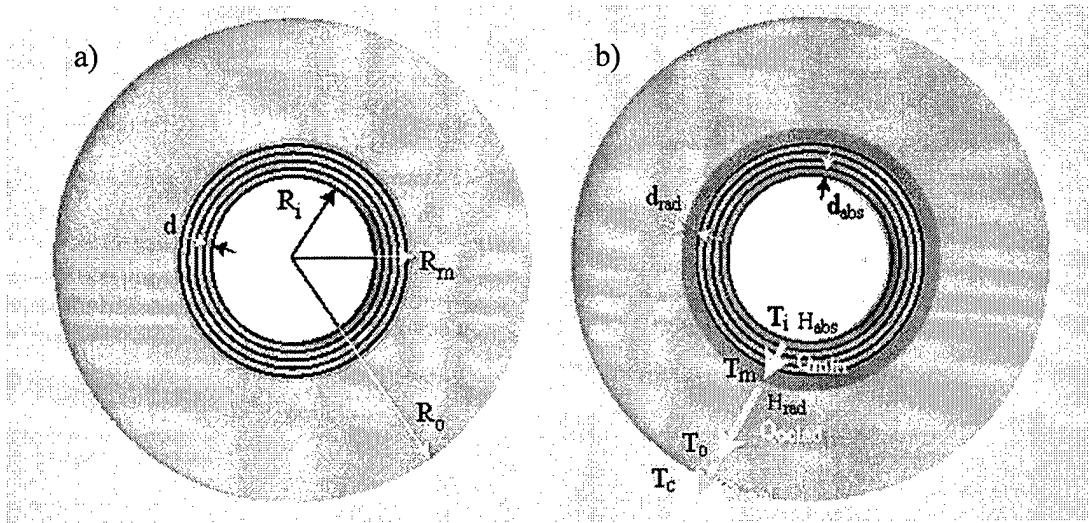
Figure 2.5.1. Power capacity analysis of a hollow Bragg fiber. (a) Schematic of a fiber. Hollow core of radius R_i, mirror region of N bilayers each of thickness d surrounded by an over-cladding extending to R_o. (b) Two major types of heat sources (shown in light gray) - H_{abs} is due to a field penetration and absorption in the mirror region, H_{rad} is due to the radiation leakage through a finite size mirror and absorption in the over-cladding.

2.5.1 Example of toolbox application: fiber heating with CW laser source (general)

We first present an analysis of the temperature increase in a fiber transmitting P [W] of power coming from a CW laser source. Cooling is provided by either dry air or water convection flow at room temperature, T_c [°C]. Heat transfer from fiber to coolant is characterized by a surface heat-transfer coefficient h [W/m^2/K]. For CW sources, the temperature rise in a fiber is very sensitive to the cooling conditions, with most of the temperature rise occurring at the cladding-air/water interface, and only a small temperature difference is observed across the fiber profile.

We assume laser beam coupling to a set of fiber modes with radial index i and angular index m, with amplitudes $C_{i,m}(z)$ along the length of a fiber. Due to modal interference, the hottest region in the fiber is not necessarily at the coupling facet, but is determined by a particular modal excitation pattern and is usually somewhere near the coupling facet. The equilibrium temperature in this region can be found by solving the time-independent heat transfer equation with insulating boundary conditions on the fiber

end facets. The heat source is computed exactly from the excited modal pattern. Energy loss in the layers with high absorption will contribute most to the heating; therefore the heat source will be a very non-uniform function in the radial direction (Fig. 2.5.2).

Figure 2.5.2. Modeling of fiber heating. Most of heating comes from energy dissipation in the mirror layers made of highly absorbing material (in red). This dissipation defines a

$$J_o=h(T(R_o)-T_{amb})$$

$J_z=0$

$J_i=0$

R_o

R_i

k – mirror heat conductance
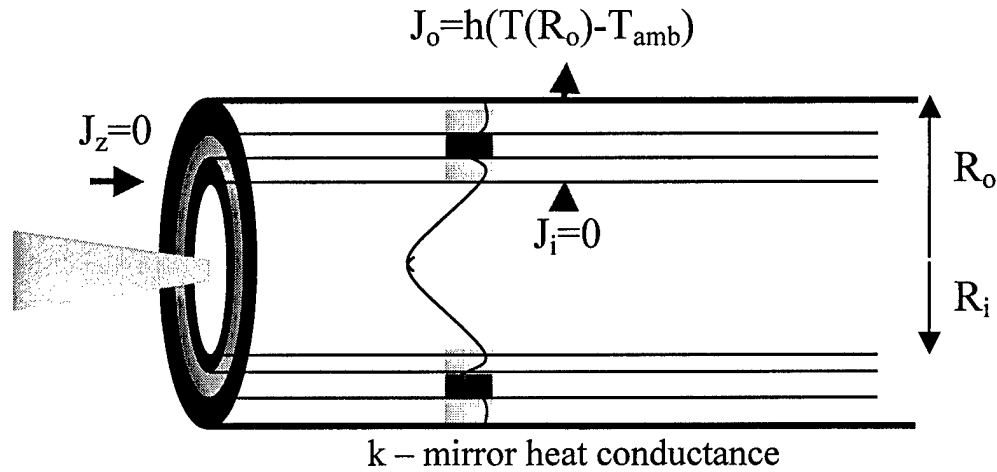
heat source very non-uniform in the radial direction. Heat conductance to the core and through the fiber end facets is assumed zero, with all the heat assumed to dissipate through the outer surface of the fiber.

In Fig. 2.5.3 we demonstrate, for example, the angle-averaged heat source arising from dissipation of the HE_{11} mode of a large core ($R_i=330\mu m$) OmniGuide chalco-polymer-polymer fiber at z = 0. As we pointed out before, most of heating comes from energy dissipation in the mirror layers made of the more highly absorbing material – the polymer. This dissipation creates a heat source that is very non-uniform in radius, with maxima in the highly absorbing layers.
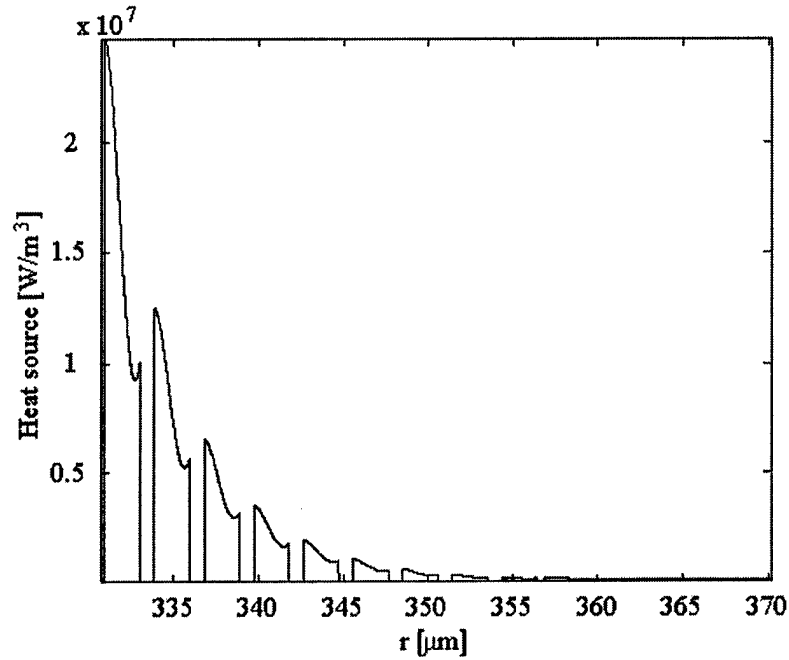
Figure 2.5.3. Heat source $S_m(\rho,z)\big|_{z=0}$ of the HE$_{11}$ mode in the fiber mirror region. Radius of the fiber core is R$_i$=330μm. All the heating comes from energy dissipation in the mirror layers made of highly absorbing material. This dissipation defines a very non-uniform heat source in radius with maxima in the highly absorbing layers. Exponential decay of the modal field inside of the reflector is responsible for most of the heat dissipated in the first few mirror layers.

In Progress Reports II and III we presented a rigorous solution of the time-independent heat flow equation with a heat source arising from absorption of the propagating modes. We also established that if interference effects can be neglected the peak temperature value T$_i$ is occurs at the inner core of the fiber end facet, and is given by

$$T_i \approx T_a + \left(\sum_{R_i\alpha_m <<1} \alpha_m P^m \right) \left(\frac{1}{2\pi R_i h} + \frac{\log\left(R_o/R_i\right)}{2\pi k_{oclad}} \right).$$

2.5.2 Example of toolbox application: increased fiber heating with CW laser source due to imperfect coupling to the HE$_{11}$ mode

In the following, we analyze the heating of the fiber when laser light is coupled through a coupler that excites higher order modes. The OmniGuide chalco-polymer-

22

polymer fiber in this example was designed for optimal performance at 10.6μm with a fiber core radius of R_i=330μm. A typical tube coupler (Fig. 2.5.4) used in our experiments consists of a short metallic tube inserted into the fiber's hollow core through a cooled metallic block.
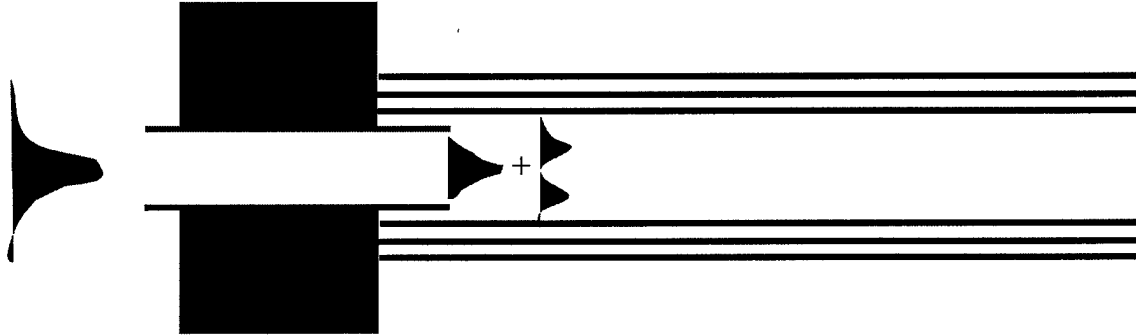

Figure 2.5.4. High power coupling to the fiber via tube coupler. Tube coupler (in blue) is inserted into the block of metal (also in blue) to shield fiber end from direct illumination by laser beam. Coupler tube is a thin metallic tube of inner core radius close to that of the fiber core radius.

Depending upon the coupling conditions, such as the diameter of the incoming Gaussian laser beam, higher order modes in the fiber can be excited. For the particular fiber/coupler geometry used in our experiments, we calculated that the incident power was distributed in the following way: 80% in the HE_{11} mode, 10% in the HE_{12} mode and the rest in higher-order modes. The losses of the HE_{11} and HE_{12} modes are 0.2 dB/m and 1 dB/m, respectively. Although the excitation of the HE_{11} mode is eight times larger than the HE_{12} mode, its losses are five times smaller then the losses of the higher order mode. Therefore the heat sources produced by dissipation of these two modes are comparable in magnitude. Moreover, because of constructive and destructive interference between the modes, the losses can vary substantially along the length of the fiber, leading to the appearance of "hot" spots. In Fig. 2.5.5 we plot temperature rise along 3m of fiber, assuming an incident power of 1W, and a surface heat transfer coefficient of h = 5 [W/m^2/K]. Note that the HE_{11} mode alone contributes 2.4 °C /W rise in temperature almost uniformly across the length of the fiber (green curve on Fig. 2.5.5), while other

excited modes have a larger contribution to the heating. Also, the temperature distribution along the fiber length is very nonuniform (red curve), with hot spots appearing about every 3cm, corresponding to the beat length between the HE_{11} and HE_{12} modes. Note also that if interference effects between modes are not taken into account, the heating profile (blue curve) only describes the average heat rise along the fiber length, totally missing the phenomenon of "hot" spots -- an important failure mechanism in high-power fibers.

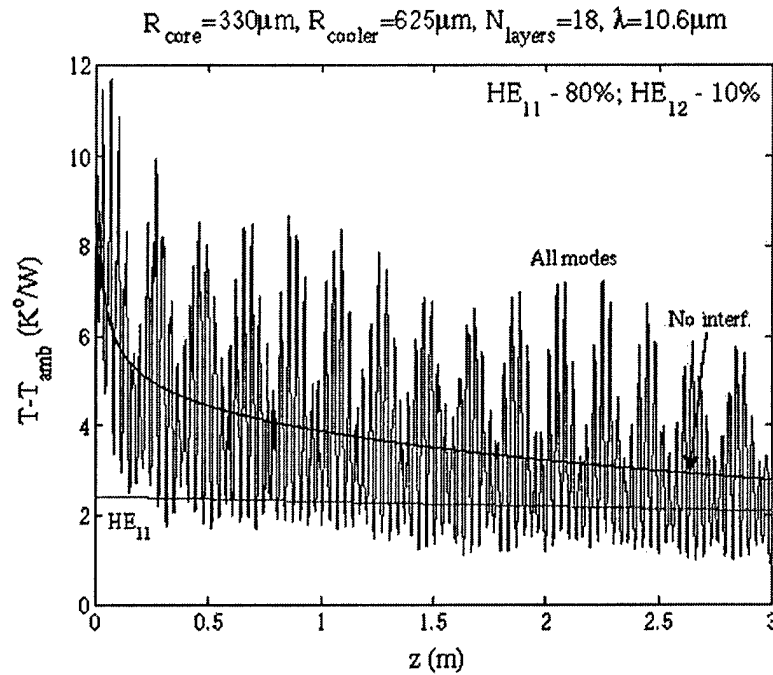$R_{core}=330\mu m$, $R_{cooler}=625\mu m$, $N_{layers}=18$, $\lambda=10.6\mu m$

Figure 2.5.5. Temperature rise per 1W of input power along a 3m fiber with heat transfer coefficient h=5 [W/m/K]. Green curve shows temperature rise when only HE_{11} mode is excited. Red curve shows temperature rise when all the modes are excited with 80% in HE_{11} mode and 10% in HE_{12} mode. Strongly oscillatory nature of the temperature distribution is due to interference between excited fiber modes. Blue curve corresponds to the temperature distribution when modal interference is not taken into account.

These predictions were tested experimentally by taking a thermal image (Fig. 2.5.6) of a short fiber piece near the tube coupler. As predicted, we see "hot" spots appearing every 2-5cm along the fiber length. A more rigorous comparison between theory and experiment is ongoing.
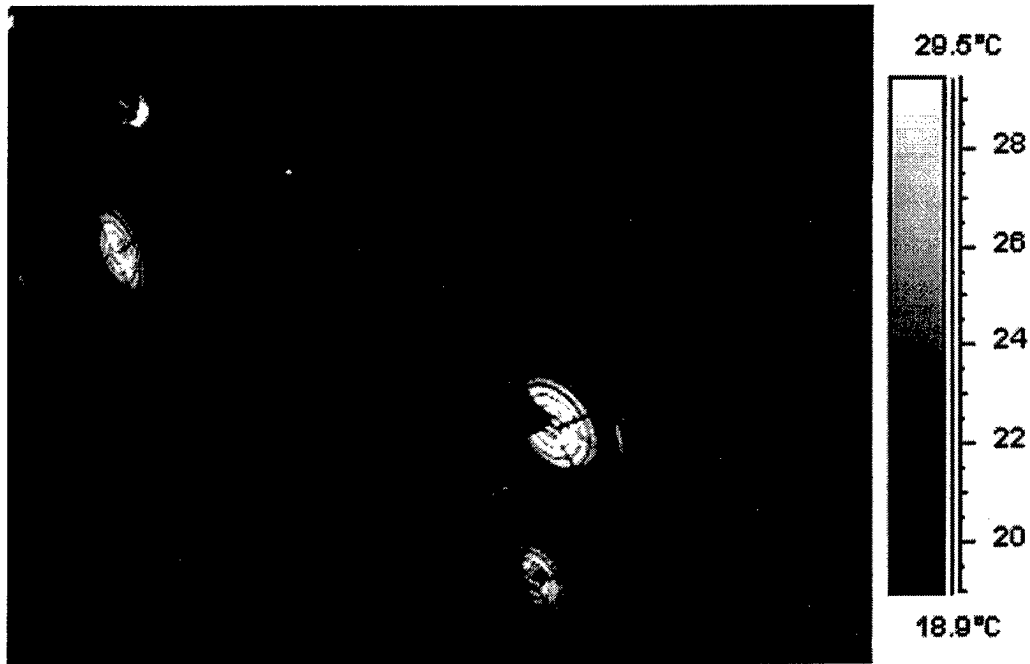
24

Figure 2.5.6. Thermal image of the 50cm fiber piece near the tube coupler with several Watts of incoming power. Note the temperature oscillations every 2-5cm appearing as "hot" spots along the fiber length. Bright light spot in the upper left corner is a reflection from the lens. Cube-shaped object close to the lens is a coupler. Bright circular objects are cooling fans with their hot motors glowing in the IR.

2.5.3 Example of toolbox application: increased fiber heating with CW laser source due to a fiber bend

When bends are present in the fiber, mode conversion is induced. The amount of this mode conversion increases with the fiber core radius. Higher order modes excited by the bend have much larger attenuation, leading to an increase in heating in the fiber bend. In Fig. 2.5.7, we show the temperature rise along a $90°$ circular bend with a 20cm bend radius. We assume an HE_{11} mode carrying 1 Watt of power is incident on the bend. At the beginning of the bend, before substantial mode conversion has occurred, heating is dominated by the HE_{11} modal loss, leading to a temperature rise of 2.4 °C/W. Further into the bend, modal conversion is substantial leading to an average temperature rise of 18

°C/W. Note the appearance of the "hot" spots along the bend length because of the modal interference.
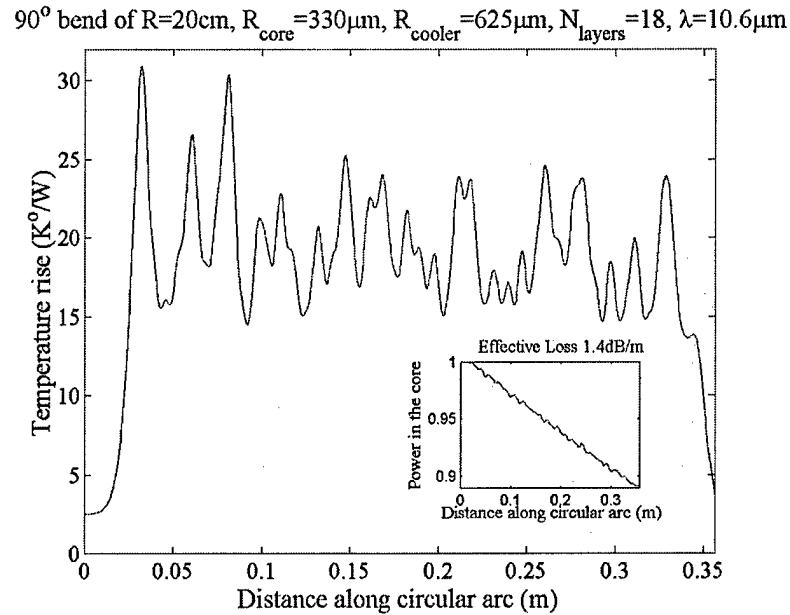

Figure 2.5.7. Heating along 90° fiber bend at 20cm bend radius, assuming excitation by HE_{11} mode with 1 Watt of power. The heat transfer coefficient h=5 [W/m/K]. At the beginning of the bend, before substantial mode conversion, heating is dominated by the HE_{11} modal loss leading to a temperature rise of 2.4 °C/W. After 2cm into the bend modal conversion is substantial leading to an average temperature rise of 18 °C/W.

2.5.4 Example of toolbox application: increased fiber heating with a pulsed laser source (general)

We now analyze the thermal behavior of an OmniGuide fiber with a pulsed power source. We assume P_{peak} [W] peak power is transmitted through the fiber with a pulse duration τ [s] and a repetition rate T [s]. We define P_{av} to be the average transmitted power: $P_{av}=P_{peak}\tau/T$. Commonly, the pulse duration is much smaller than the characteristic temperature equilibration time across the fiber cross-section $\tau_{eq}=C_v\rho R_i^2/k$. In this short pulse regime, the temperature distribution across the fiber cross-section will be modified from that of the steady-state distribution corresponding to the average

transmitted power P_{av}. In general, power handling of a pulsed source is more challenging than power handling of CW radiation of the same average intensity. Physically, this can be attributed to the excitation by a time-dependent source of localized "heat waves" (Figure 2.5.8).
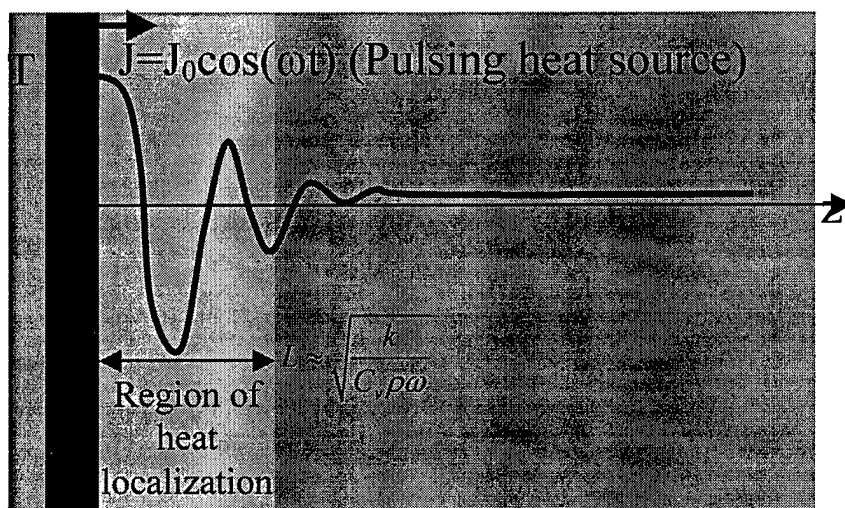

Figure 2.5.8. Phenomenon of "heat wave". Heat dissipation from a temporally periodic heat source deteriorates as temporal frequency of the source gets larger, leading to an increase in local heating. Heat from a time dependent source is localized inside of a region of size L, inversely proportional to the square root of the source frequency.

The larger the frequency of the heat source, (i.e., the shorter the pulse duration) the more localized is the "heat wave", thus weakening heat exchange through the outer boundary of the fiber to the surrounding coolant. For the very lossy cladding modes, heating becomes even more problematic because of the additional localization of the heat in the direction of propagation due to the very rapid modal decay. Special care should be taken to reduce coupling to the cladding modes.

As in the analysis of CW sources, we assume laser beam coupling to a set of fiber modes with radial index i, angular index m, and frequency ω, with excitation coefficients $C_{i,m}(z)$ along the length of the fiber. The steady-state temperature in the fiber can be found by solving the time-dependent heat transfer equation with boundary condition of zero flux across the fiber side facets. The heat source is computed exactly from the excited modal pattern.

27

In Progress Report III, we presented a rigorous solution of the time-dependent heat flow equations with a heat source arising from absorption of the propagating modes.

2.5.5 Example of toolbox application: heating due to pulsed sources in chalco-polymer-polymer OGCI fibers

In Progress Reports II and III, we established that, neglecting modal interference, the hottest region of the fiber is on the coupling facet of the fiber at the core/mirror boundary. The peak temperature value T_i in this region over time was approximated by solving a simplified time-dependent heat transfer equation with boundary conditions of zero flux across the coupler/fiber facet and the end facet, and by assuming that all the heat flux was coming into the fiber from a very narrow heat source at the fiber core/mirror boundary. The maximum temperature was then established to be

$$T_i \approx T_a + \left(\sum_{R_i \alpha_m \ll 1} \alpha_m P_{av}^m \right) \left(\frac{1}{2\pi R_i h} + \frac{\log(R_o / R_m)}{2\pi k_{oclad}} + 0.84 \frac{\frac{1}{\nu}\sqrt{\frac{k_{oclad}}{\tau C_\nu \rho R_i^2}}}{2\pi k_{oclad}} \right).$$

Thus, assuming that high-loss cladding modes $R_i \alpha_m \gg 1$ are suppressed, the temperature rise for the pulsed source as a function of the average power, pulse duration and pulse repetition rate will be given by a universal curve in coordinates $(\frac{1}{\nu\sqrt{\tau}}, \frac{T_i - T_a}{P_{av}})$.

In these coordinates, the temperature rise is given by a family of straight lines each corresponding to a different cooling mechanism. The CW power capacity is calculated by letting $\frac{1}{\nu\sqrt{\tau}} = 0$. For example, a chalco-polymer design with R_i=330µm and 14 bilayers, a maximum allowed temperature rise of ΔT=150°C, dry air cooling, with HE_{11} mode propagation, has a CW power capacity of P_{av}=73W . The CW temperature rise of this fiber will be T_{CW}=2°C/W. For a pulsed cutting laser with τ=200ns and ν=100Hz, the maximum power capacity is reduced to P_{av}=62W, with P_{peak}=3·10⁶W.

The rigorous calculation of thermal behavior with pulsed sources described in Progress Report III shows that the temperature rise is actually smaller when evaluated with a realistic heat source, rather than a δ-function-like heat source. For example, for the same chalco-polymer-polymer design, as the repetition rate of the pulses increases, the temperature distribution tends to get closer to the CW distribution with the same average power. In Fig.2.5.9 we present the temperature rise due to a pulsed source as a function of the pulse parameter $\dfrac{1}{v\sqrt{\tau}}$. The simplified theory with a δ-function-like heat source predicts a straight line. Detailed calculations show that this line gives an upper bound on the actual heating due to a pulsed source. In reality, because of the finite extent of the heat source, the temperature rise curves tend to a CW temperature rise as the pulse repetition rate increases. In Fig.2.5.9, several temperature rise curves are presented as a function of $\dfrac{1}{v\sqrt{\tau}}$. They are labeled and calculated for particular pulse repetition rates v, where the pulse duration τ is varied.

Manufacturing target structure R_{core}=330μm, R_{clad}=625μm, HE_{11} mode of 0.2dB/m loss
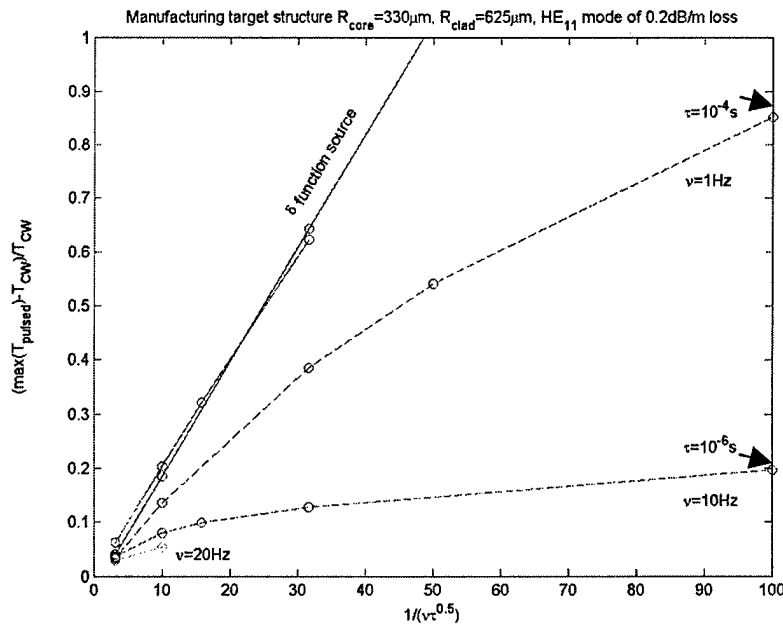

Figure 2.5.9. Temperature rise curves as a function of the laser pulse parameter; v is the pulse repetition rate, τ is the pulse duration. Different dashed curves are calculated for a realistic heat source, and correspond to different pulse repetition rates. Solid blue curve is

29

calculated for a simplistic δ–function like heat source which provides an upper bound on the heating increase due to pulsed sources.

2.6 Toolbox: $HE_{11} \rightarrow TE_{01}$ modal conversion

Input: fiber geometry, parameters of a serpentine mode converter. Serpentine mode
      converter is characterized by the pitch, amplitude, and length of the incoming and
      outgoing transition regions.

Output: amplitudes of excited modes.

As described in detail in Progress Report I, the HE_{11} and TE_{01} modes are the most desirable for operation in an OmniGuide fiber. The HE_{11} mode has the best coupling to a Gaussian laser beam, while the TE_{01} mode has the lowest transmission loss, but, unfortunately, does not couple well to an incident laser beam. With a low-loss $HE_{11} \rightarrow TE_{01}$ mode converter, however, the HE_{11} mode can be employed for efficient coupling, and the TE_{01} mode can be used for optimal transmission. We have successfully initiated a theoretical and experimental effort to develop a mode converter that efficiently performs this conversion in an OmniGuide fiber.

2.6.1 Example of toolbox application: HE_{11} (LP_{01})→TE_{01} (LP_{11}) modal conversion in SMF-28 fiber at λ=633nm

A prototype mode converter that we studied consists of a deformation of the fiber axis into an appropriate serpentine bend. This deformation is achieved by pressing the fiber between two sets of wires wrapped on two cylinders (Figure 2.6.1). The wire diameter is chosen so that the bend spacing in the fiber axis matches the beat length between the HE_{11} and TE_{01} modes. Initially, all the power is launched into the HE_{11} mode. If the diameter of the wire matches exactly the beat length between the modes, almost 100% conversion efficiency can be achieved by varying the pressure on the top set of wires to induce the proper deformation. In practice, this matching condition is hard to achieve, so conversion efficiency is usually smaller.
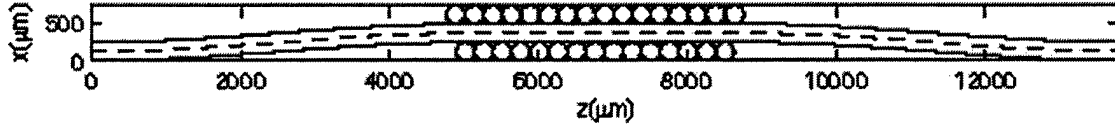
Figure 2.6.1. Mode converter induces a serpentine 2D bend by pressing the fiber between two sets of wires wrapped on two cylinders. The diameter of wires is matched to the beat length between two modes. Amplitude of fiber oscillations δ is chosen to optimize mode conversion.

In Figure 2.6.2 we present simulations of the maximum converter efficiency based on a specialty step-index silica fiber operating at $\lambda=633$nm. At this wavelength, the specialty fiber has a single HE_{11} (LP_{01}) mode and three almost degenerate LP_{11} modes, one of which is the TE_{01}, above cutoff. The fiber has a core radius of $R_c=2.23$ μm, and an index contrast $\Delta n/n_c=0.34\%$. The beat length between the HE_{11} and TE_{01} modes for this fiber is 247 μm. In the experimental realization of the mode converter, 14 consecutive wire wraps of diameter D=254 μm were employed.
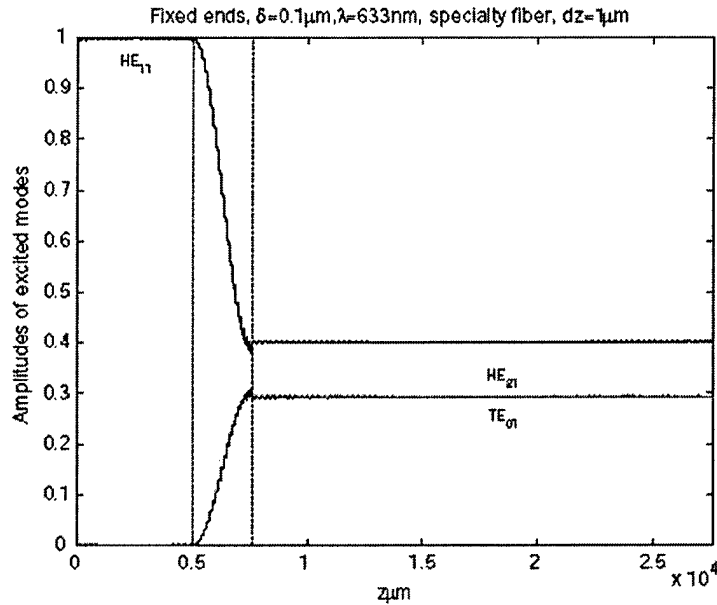

Figure 2.6.2. Mode conversion in a serpentine 2D bend along the length of a converter. Polarization of the initial HE_{11} mode corresponds to $E \perp$ to plane of the bend. Maximum 58% mode conversion into LP_{11} is predicted with 29% ending up in the TE_{01} mode for the optimal amplitude of fiber bend oscillation of $\delta=100$nm.

31

We used in-house software to extract the modal content from intensity images of the converter output that were recorded by a CCD camera. From the experimental images, (Figure 2.6.3) we found that we achieved 55% conversion into the LP_{11} group, which agreed very well with the predicted conversion rate.
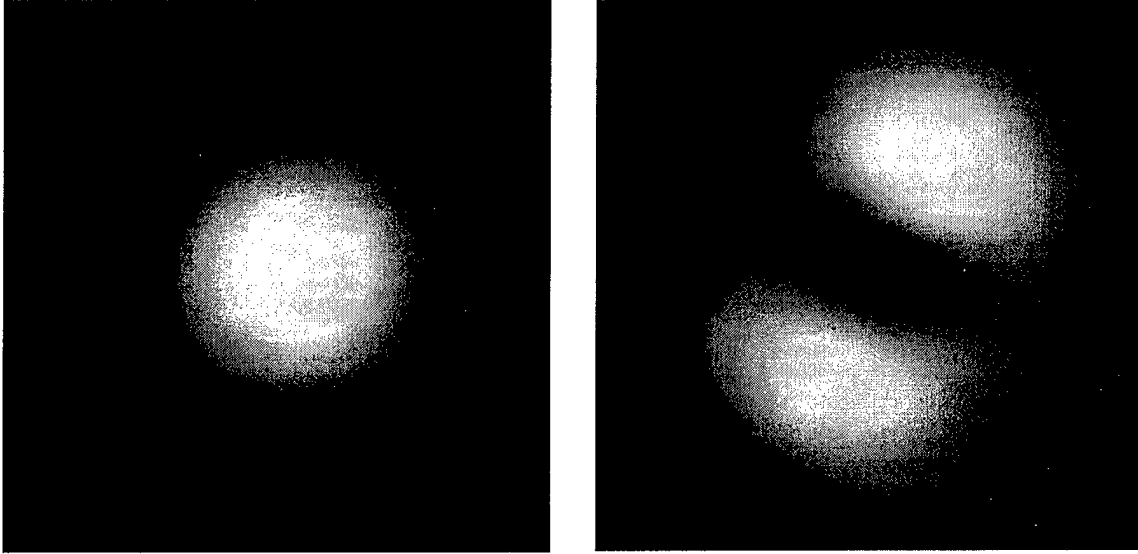

Figure 2.6.3. CCD images of mode conversion in a serpentine 2D bend. Left – HE_{11} mode in initial unperturbed SMF-28 fiber. Right – mode conversion by gently pressing on the top set of wires – maximum conversion of 58% into LP_{11} achieved by varying the pressure on the top set of wires.

2.7 Toolbox: Beam Propagation Method

Input: description of the fiber, description of (gentle) imperfections along the direction of propagation. The incoming profile of the electromagnetic field has to be provided to start the propagation. The BPM software has its own interface based on the programming language Guile.

Output: electromagnetic fields along the direction of propagation.

The general problem of field propagation through an index profile with arbitrary (but slowly-varying) perturbations can be in many cases be addressed by the Beam

Propagation Method (BPM). Currently, all finite-difference BPM codes of which we are aware, including commercially available codes, are unstable when applied to the study of high index contrast systems – the computed fields grow arbitrarily large during propagation. While there is some evidence of stable Finite Element BPM codes, they are not yet in the public domain and are definitely not optimized for the study of high index contrast, multi-layered index profiles. We have developed BPM software that is numerically stable and includes a wide angle correction based on 1st and 2nd order Pade expansions. This toolbox allows us to study complex devices built out of OmniGuide fibers, as well as analyze the effects of imperfections present in these fibers.

2.7.1 Example of toolbox application: field propagation in fiber with microbending

A common imperfection in a fiber is microbending. We present simulation results of TE_{01} mode propagation through an S-shaped microbend with bending radius R_{bend}=500μm and bending angle of 12°. The OmniGuide fiber has a core radius of 2.5μm and 7 mirror layers optimized for transmission at 1.55μm. In Fig. 2.7.1 we show snapshots of the TE_{01} energy density in the fiber cross-section along the bend. The BPM calculation predicts a 2dB loss from the bend.
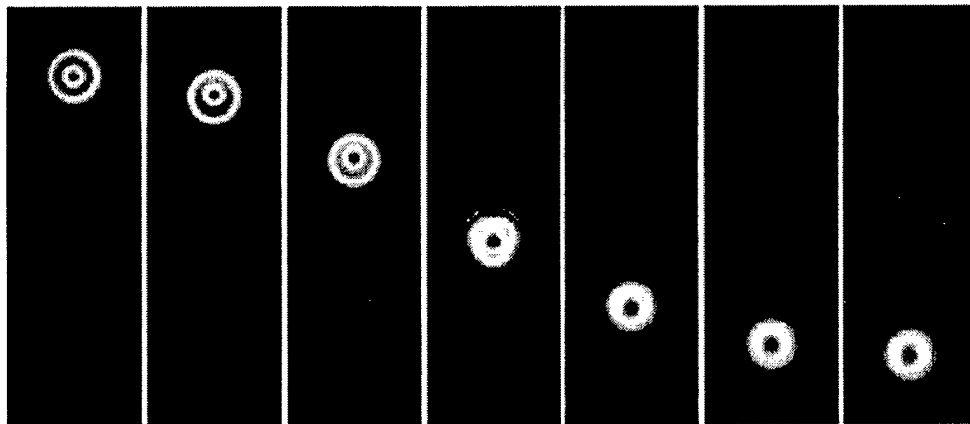

Figure 2.7.1. Energy dissipation of TE_{01} mode in an S-bend with R_{bend}=1000μm and bending angle of 12°. A sequence of energy density snapshots in the fiber cross section along the fiber is presented. Outmost left picture corresponds to the starting energy density before the bend. Outmost right picture corresponds to energy density after the bend. Colorscale is red-maxumum energy density, white-minimum.

2.7.2 Stability analysis of BPM code (The work presented in this section was performed by Stanford University)

The effect of the Crank-Nicolson α parameter on the numerical stability and dissipation of the OGBPM simulation code has been investigated. Field propagation in the OGBPM is accomplished with the Crank-Nicolson method, and it is employed as follows:

$$\frac{\partial F(z)}{\partial z} = \hat{O}(z)F(z)$$

$$F(z+dz) = (1 - dz\alpha\hat{O}(z+dz))(1 + dz(1-\alpha)\hat{O}(z))F(z)$$

where dz is the step size in the direction of propagation through which the field F is advanced.

In the following, we investigate the performance of the OGBPM code as a function of the Crank-Nicolson parameter α. Previously, we observed that stability of OGBPM can be substantially improved by increasing α from its ideal value of ½, where the Crank-Nicolson algorithm is second-order accurate. However, when α is changed from its ideal value, numerical dissipation is introduced into the system. Moreover, numerical convergence also suffers, with the error of the method now being proportional to dz rather than dz^2 for $\alpha = 1/2$. The purpose of this report is to investigate these tradeoffs between numerical stability and numerically induced dissipation.

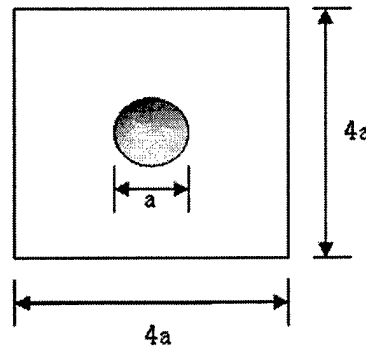To investigate the effect of the α parameter, an index guided fiber is considered (Fig.4.1).

Figure 2.7.2 4a ×4a computational cell, dielectric cylinder ($\varepsilon = 11.56$) with diameter a, in vacuum.

The initial field profile is imported from the MIT Photonic Band (MPB) simulation code with the same fiber structure. The frequency is set to the eigen-frequency of the mode (0.357954). The wavevector is set to 1 as in the MPB simulation. The following are typical distance vs. total energy plots after propagation of the initial field by OGBPM (Fig. 2.7.3)
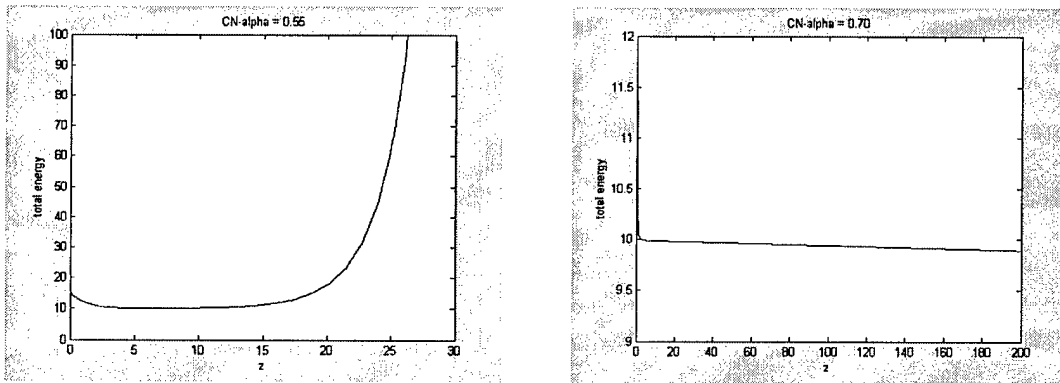

Figure 2.7.3. Distance vs. total energy plots after propagation of initial field by OGBPM. Diverging ($\alpha = 0.55$) and non-diverging ($\alpha = 0.70$) examples.

The initial drop in energy is possibly due to a mode mismatch between the MPB code and OGBPM. One can fit the decay (growth) in both cases with exponential functions of the form A*exp(Bz). In both cases, a very good fit is achievable, indicating that the decay (growth) is typical numerical divergence / dissipation (Fig. 2.7.4).
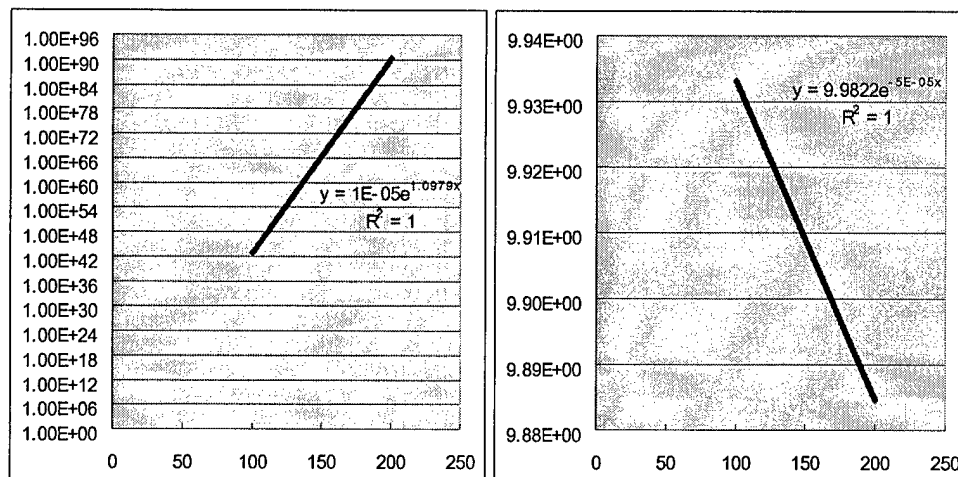
Figure 2.7.4. Fit of the energy decay curves with exponential functions of the form A*exp(Bz).

The relationship between α and the growth/decay constant B is summarized in the tables below. Observe that α=0.62 provides stable propagation with no dissipation. Choosing α>0.62 leads to a stable propagation scheme, but an artificial numerical dissipation is introduced. Choosing α<0.62 leads to an unstable propagation scheme.

α	0.5	0.6	0.7	0.8	0.9	1
A	1.00E-05	4.00E-04	9.9821	9.9821	9.9819	9.9817
B	1.0962	0.0389	-5.00E-05	-7.00E-05	-1.00E-04	-1.00E-04
R^2	1	0.9984	1	1	1	1

α	0.55	0.56	0.57	0.58	0.59	0.6	0.61	0.62
A	1.00E-05	1.00E-05	1.00E-05	1.00E-05	3.00E-05	4.00E-04	9.98E+00	9.98E+00
B	0.5755	0.4691	0.3634	0.2574	0.148	0.0389	-3.00E-05	-3.00E-05
R^2	1	1	0.9999	0.9999	0.9992	0.9984	0.9995	1

3 References

1. Winn J.N., Fink Y., Fan S.H., Joannopoulos J.D.," Omnidirectional reflection from a one-dimensional photonic crystal," Optics Letters, vol. 23, pp. 1573-1575, 1998

2. Yablonovitch E., "Engineering omnidirectional external-reflectivity spectra from one-dimensional layerd interference filters," Optics Letters, vol. 23, p. 1648, 1998

3. Pochi Yeh, Amnon Yariv, and Emanuel Marom, "Theory of Bragg fiber," J. Opt. Soc. Am., vol. 68, 1996, 1978

4. Yoel Fink, Joshua N. Winn, Shanhui Fan, Chiping Chen, Jurgen Michel, John D. Joannopoulos, Edwin L. Thomas, "A Dielectric Omnidirectional Reflector," Science, vol. 282, p. 1679, 1998

5. US Patent: J.D. Joannopoulos, S. Fan, J.N. Winn, Y. Fink, "High Omnidirectional Reflector," # 6,130,780

6. Deopura M, Ullal CK, Temelkuran B, Fink Y., "Dielectric omnidirectional visible reflector," Opt. Lett., vol. 26, pp.1197-1199, 2001

7. Temelkuran B., Thomas E.L., Joannopoulos J.D., Fink Y., "Low-loss infrared dielectric material system for broadband dual-range omnidirectional reflectivity", Opt. Lett., vol. 26, pp. 1370-1372, 2001

8. Marcatili E.A, and Schmeltzer R.A, "Hollow metallic and dielectric waveguides for long distance optical transmission and lasers," The Bell System Technical Journal, p. 1783, July 1964

9. Pochi Yeh, Amnon Yariv, and Chi-Shain Hong, "Electromagnetic propagation in periodic stratified media. I. General theory," J. Opt. Soc. Am., vol. 67, p. 423, 1977

10. A.N. Lazarchik, "Bragg fiber lightguides," Radiotekhnika I Electronika, vol. 1, pp. 36-43, 1988

11. Johnson SG, Ibanescu M, Skorobogatiy M, Weisberg O, Engeness TD, Soljacic M, Jacobs SA, Joannopoulos JD, Fink Y," Low-loss asymptotically single-mode propagation in large-core OmniGuide fibers," Optics Express, vol. 9, pp. 748-779, 2001

12. B.Z. Katsenelenbaum, L. Mercader del Rio, M. Pereyaslavets, M. Sorolla~Ayza, and M. Thumm, "Theory of nonuniform waveguides: the cross-section method," Inst. of Electrical Engineers, London, 1998

13. M. Skorobogatiy, Mihai Ibanescu, Steven G. Johnson, Ori Weisberg, Torkel D. Engeness, Marin Soljacic, Steven A. Jacobs, and Yoel~Fink, "Analysis of general geometric scaling perturbations in a transmitting waveguide. The fundamental connection between polarization mode dispersion and group-velocity dispersion," JOSA B, vol. 19, p. 2867, 2002

14. Steven G. Johnson, M. Ibanescu, M. Skorobogatiy, O. Weisberg, J.D. Joannopoulos, and Y. Fink, "Perturbation theory for Maxwell's equations with shifting material boundaries," Phys. Rev. E, Vol. 65, p. 66611, 2002

15. At OmniGuide, we are currently investigating two different mirror designs. Both employ chalcogenide glass for the high index layer. One design also uses a

chalcogenide glass for the low index layer and the other uses a polymer. Properties of the materials are as follows:

		Polymer	Chalco Glass
Wavelength	λ [μm]	2-11	2-11
Index of refraction	N	1.5	2.3-2.8
Bulk material absorption	α [dB/m]	10^5	1 0
Heat conductivity	K [W/m/K]	$0.16 - 0.27$	0.252
Density	ρ [kg/m^3]	1400	4400
Specific heat	C_v [J/kg/K]	1000	294

16. Abel, and Harrington, Appl. Opt., vol. 34, p. 6642, 1995